

A Dissipation-Based Method for Improving the Accuracy of Computational Fluid Dynamics Simulations of High Level Non-Newtonian Wastes

Ahmad Abbasi Baharanchi^{*,1,2}, Maximiliano Edrei^{1,2}, Seckin Gokaltun¹, Dwayne McDaniel¹

¹Applied Research Center, Florida International University, Florida, United States

²Department of Mechanical and Materials Engineering, Florida International University, Florida, United States

Abstract

This paper investigates a new viscosity model for laminar, transitional, and turbulent pipe flow simulations of a non-Newtonian slurry using the Star-CCM+ software. Herschel-Bulkley (HB) rheology equation was used in its original and modified forms to model the fluid viscosity. The realizable k- ϵ model was used for modeling of turbulence. It was observed that simulations using the HB model predicted inaccurate profiles of U (mean velocity) and U^+ (mean velocity in wall units). Therefore, we developed alternative values of viscosity obtained directly from non-linearity of stress-strain variation (α) in each iteration. The developed method, “Alpha method”, applied changes in places where dissipation rate of turbulent kinetic energy occurred and was designed based on local or global dissipation rate values. Inverse values of α were used to test effects of more viscosity reduction for all flow regimes. In prediction of the mean velocities, significant improvements were obtained through global adjustment of viscosity in inverse form during simulation of the laminar and turbulent flow cases. For the transitional flow, obtaining improvements in prediction of U and U^+ from the same model version faced challenges. While the global adjustments in direct form were found significantly effective in improving the prediction of U , they failed to predict the U^+ accurately. For this purpose, Local viscosity adjustments were found significantly effective.

1. Introduction

Presently millions of gallons of radioactive waste are stored in underground tanks at various U.S Department of Energy (DOE) sites (Gokaltun et al. [8]) and DOE is in the process of transferring the waste from single shell tanks to double shell tanks (Meyer et al., [11] and Gokaltun et al. [8]). Meyer et al. [11] introduced two types of simulants for the PJM systems in the Hanford site 1) a Laponite-based simulant with the Laponite concentration typically about 2 wt% and the density slightly greater than that of water, 2) a Kaolin-bentonite simulant with 80% kaolin and 20% bentonite powder mixed to various solids concentrations in water. Simulant development efforts are summarized in their work and in Poloski et al. [12]. Peltier et al. [13] considered the 1.5 wt% Laponite-based simulant for the slurry in PJM systems, which according to Escudier and Presti [6], obeys the Herschel–Bulkley rheological model.

* Corresponding Author: Tel: 305-879-4856, Fax: 305-348-1852, aabba003@fiu.edu.

Literature contains a number of valuable experimental investigations on non-Newtonian fluids such as given in Bingham [3], Dodge and Metzner [5], Thomas [18-19], Pinho and Withelaw [14], Escudier and Presti [6], Poloski et al. [12], and Meyer et al. [11]. Some of these investigations, such as the ones by Bingham [3], Herschel and Bulkley [10] and Cross [4], led to the development of popular viscosity models for non-Newtonian fluids that are extensively used in computational investigations today; however, according to Gavrilov and Rudyak [9], the amount of available experimental data on non-Newtonian flows is insignificant compared to the exploding efforts using numerical simulations.

There have been valuable efforts published in the literature to improve the accuracy of numerical algorithms in the prediction of flow characteristics of Non-Newtonian fluids. Wilson and Thomas [20] improved the theory of the Power-law and Bingham plastic fluids for the log-law region of the velocity profile towards better prediction of the wall friction coefficient. Their analysis was based on the drag reduction associated with non-Newtonian fluids and colloidal suspensions, as was first reported by Toms [17], according to Andrade et al. [1]. This modification reflected enhanced viscosity effects for dissipative micro-eddies that possess small time and length scales. Soto and Shah [15] developed an algorithm for the simulation of an entrance flow of a yield-power-law fluid, which produced results in good agreement with analytical solutions for different yield stress and power-law exponents. Bartosik [2] applied the theory of Wilson and Thomas [20], which described the change of the boundary layer thickness and suppression of turbulence in the boundary layer for the slurry flow with very fine solid particles. Bartosik [2] employed a $k-\epsilon$ turbulence model with modified damping functions and compared the performance of power-law and Herschel and Bulkley (HB) models in the simulation of a Kaolin slurry. He found that HB model better describes the shear stress at the low shear deformation rate. Gavrilov and Rudyak [9] improved the prediction of a specific $k-\epsilon$ turbulence model by adding an extra term to the definition of the shear rate and obtained results in close agreement with data obtained from a direct numerical simulation (DNS) study; however, applicability of this model to laminar flow is questionable due to its dependence on the dissipation rate of the turbulent kinetic energy.

Despite these significant contributions, there is still a need to find a universal model to define the viscosity properly in the entire computational domain for different regimes of the flow in a wide range of Reynolds numbers so that its applicability is not specific to a flow with certain material, geometry, and boundary conditions. One possible approach is to dynamically modify the viscosity during simulation. In this study, two different ways of achieving this goal were implemented. In the first approach, the parameters that affect the viscosity were modified. This approach was pursued in some studies mentioned in review of the literature earlier, such as the method of Gavrilov and Rudyak [9] which was designed to alter viscosity by correcting the definition of the shear rate. In the second approach, viscosity was directly altered following a specific algorithm, which is based on energy dissipation rate in non-linear fluids. We pursued the

second approach in this paper and developed an algorithm based on the Herschel and Bulkley (HB) [10] model of viscosity. Our goal was to improve predictions of k-ε turbulence model when modifications were applied to the entire computational domain. Improved results for transitional and turbulent regimes with Reynolds number ranging between 3,400 to 25,300 were obtained.

2. Theory and Hypothesis

According to Escudier et al. [7] and Meyer et al. [11] the slurry fluid in Hanford site can be categorized as a viscoplastic material. **Fig. 1** shows the non-linear variation of the stress against the strain rate after the yield stress is achieved in the flow.

[Place Fig. 1 here.]

The mathematical expression for this stress-strain relationship is shown in Eq. (1).

$$|\tau| = \tau_Y + k \dot{\gamma}^n \quad (1)$$

In this expression, τ , τ_y , k , $\dot{\gamma}$, and n are the shear stress, the yield shear stress, the consistency, the shear rate, and the power exponent, respectively. In addition, $|\tau|$ shows the magnitude of the shear stress. On this graph, it is possible to connect any point to the origin and create a rectangular area under the stress-strain curve. The straight line shown in Fig. 1(a) connects an arbitrary point on the curve to the origin and we called the slope of this line as the pseudo-Newtonian viscosity, for similarity to the linear stress-strain relationship in Newtonian liquids. This slope is different from the tangential viscosity of the fluid since the tangential viscosity is the slope of the line tangent to the profile at any arbitrary point, e.g., the red line. The term “pseudo-Newtonian” is used since this scholar represents an imaginary Newtonian liquid which is constructed from the rheogram of a non-Newtonian fluid. Similarly, we call the straight line as the pseudo-Newtonian line.

Later, it is possible to define a coefficient, α , as the ratio of the area under the stress-strain curve of a viscoplastic fluid, i.e., $S1+S2$, to the area under the pseudo-Newtonian line, i.e., $S1$, as shown in **Fig. 1** and expressed by Eq. (2).

$$\alpha = \frac{S1+S2}{S1} \quad (2)$$

According to Wilson and Thomas [20], the area under the stress-strain curve represents the typical rate of energy dissipation in the flow. Therefore, α represents the ratio of the dissipation rates of the energy for non-Newtonian fluid over the pseudo-Newtonian fluid. We used the term “non-linearity coefficient” for α as it shows the deviation of the energy dissipation of a non-Newtonian fluid from that of a Newtonian fluid. The theory of Wilson and Thomas [20] states that as far as dissipative eddies of a turbulent flow are concerned, the non-Newtonian fluid acts as if it were a Newtonian liquid with a substitute viscosity of $\alpha \times \eta$, where η is the pseudo-Newtonian viscosity. Therefore, utilization of this substitute viscosity for the entire range of dissipative eddies in the turbulent flow will cause the same dissipation rate of energy occurring to the non-Newtonian fluid. The requirement of this method is that the value of the substitute viscosity must be updated in every iteration of the numerical solution. This in turn requires reevaluation of α and η after every iteration. This method is similarly applied to laminar flows in the absence of eddies, since dissipation of energy occurs by the action of viscosity regardless of the flow regime.

Eq.(3) shows the mathematical expression for the local version of alpha quantity. This definition is based on the fact that the areas named as S1 and S2 could be constructed at any point on the profile of the rheogram. Based on this definition, for any points considered on the rheogram profile, equal values of energy dissipation would be obtained if a Newtonian liquid with substitute viscosity of $\alpha \times \eta$ was used. It must be noted that in every iteration, a new rheogram will be obtained from the solution of flow equations and the solution will dynamically adapt to the new rheogram. The expression to the right of the second equality sign in Eq.(3) was obtained by replacing the stress term from Eq. (1). More derivations led to a simple expression for local value of α , i.e., α_{loc} , as shown in Eq. (4).

$$\alpha_{loc} = \frac{\int_0^Y (\tau dY)_{HB}}{0.5 \times (Y)_{HB} \times (\tau)_{HB}} = \frac{\int_0^Y [(\tau_y + k Y^n) dY]_{HB}}{0.5 \times (Y)_{HB} \times [(\tau_y + k Y^n)]_{HB}} \quad (3)$$

$$\alpha_{loc} = 2 \times \frac{\tau_y + \frac{k (Y)^n}{n+1}}{\tau_y + k (Y)^n} \quad (4)$$

The term “local” was used since no special point on the rheogram profile was considered. This equation shows that alpha depends on one variable only. i.e., the local shear rate (Y), and other quantities, such as yield stress (τ_y), are constant parameters. We evaluated this relationship for a wide range of variation of Y and, as is shown by **Fig. 2**, a small variation of α in the range of 1.3 to 2 was observed.

[Place Fig. 2 here.]

Later, by utilizing the well know shear-strain relationship, i.e., $|\tau| = \mu \times \dot{\gamma}$, we defined a pseudo-Newtonian viscosity as the slope of the hypotenuse of S1 triangle shown in rheogram of Fig. 1. This quantity is expressed by Eq. (5).

$$\mu_{\text{pseudo_Newt.loc}} = \frac{\tau_{\text{HB}}}{\dot{\gamma}} = \frac{\tau_{\dot{\gamma}}}{\dot{\gamma}} + k \dot{\gamma}^{(n-1)} \quad (5)$$

Next, by considering the entire area under the profile of rheogram, which is from the origin to the apex point on the curve, an expression for Global value of alpha was derived, as is shown by Eq. (6). The subscript ‘‘max’’ refers to the apex on the rheogram profile, since at this especial point stress and strain rate are both maximum. The slope of the straight line that connects the apex to the origin is the pseudo-Newtonian-Global viscosity and is expressed by Eq. (7).

$$\alpha_{\text{Global}} = 2 \times \frac{\tau_{\dot{\gamma}} + \frac{k (\dot{\gamma}_{\text{max}})^n}{n+1}}{\tau_{\dot{\gamma}} + k (\dot{\gamma}_{\text{max}})^n} \quad (6)$$

$$\mu_{\text{pseudo_Newt.Global}} = \frac{\tau_{\text{HB_max}}}{\dot{\gamma}_{\text{max}}} = \frac{\tau_{\dot{\gamma}}}{\dot{\gamma}_{\text{max}}} + k \dot{\gamma}_{\text{max}}^{(n-1)} \quad (7)$$

According to Wilson and Thomas [20], dissipation can occur in the entire computational domain and predominantly in the viscous sub-layer, where only dissipative eddies can be present. Therefore, by using the substitute viscosity for the dissipative scales, it is possible to modify the viscosity in the entire domain in an iterative and corrective fashion. This modification is not needed for the inertia eddies since large eddies do not participate in viscous dissipation. Therefore, a model with the following formulation is proposed.

$$\mu_{\text{alpha.dir.}} = \begin{cases} \mu_{\text{HB}} = \frac{|\tau|}{\dot{\gamma}} = \frac{\tau_{\dot{\gamma}}}{\dot{\gamma}} + k \dot{\gamma}^{(n-1)} & \varepsilon_{\text{H-B}} \leq \varepsilon - \text{THS} \\ \alpha \times \mu_{\text{pseudo_Newt.}} & \varepsilon_{\text{H-B}} > \varepsilon - \text{THS} \end{cases} \quad (8)$$

This version of the alpha model is called here as *Direct-Alpha viscosity model* or shortly *Direct-Alpha model*, since the coefficient α is directly applied to the modeling. We will later challenge this application by using inverse of the α in the modeling.

The HB viscosity, as is defined on the first line of the Eq. (8), is obtained by using the shear-strain relationship, i.e., $|\tau| = \mu \times \dot{\gamma}$, imposed on the Eq. (1). This viscosity function is provided to the Star-CCM+ as part of the input property of the fluid. The parameter ε -THS is defined as the threshold for the dissipation rate. We set this threshold to zero to engage the entire dissipation range (all dissipative scales) in the modification of viscosity. However, sensitivity of the

model can be further reduced by increasing the ε -THS values. In the laminar flow simulation, the entire domain will be affected. In addition, two versions of the model can be produced by using the global or local values of α and $\mu_{\text{pseudo-Newt.}}$

The following algorithm is executed to implement the alpha method in the Star-CCM+ CFD application:

1. Initialize the solution with a constant viscosity
2. Update the entire flow field by solving the governing equations
3. Switch to the Herschel-Bulkley method
4. Update the entire flow field by solving the governing equations
5. Update the rheogram and correct the viscosity
6. Go to step 4 and continue until converged solution is obtained.

3. Governing Equations

Governing equations of the turbulence model and the method of Gavrilov and Rudyak [9] are briefly explained. Eqs. (9-13) show the expressions for the conservation of continuity and momentum and the k- ε model for an incompressible flow. In these equations all vectors and scalars represent mean field variables except for the primed variables, which represent fluctuations. The values of model constants, σ_k and σ_ε , in Star-CCM+ are 1.0 and 1.3, respectively. In addition, μ_t is the turbulent viscosity defined by $\mu_t = \rho C_\mu k T$, where, the values of C_μ is 0.09, and T is the turbulent time scale defined by Eq. (15).

$$\frac{\partial(\rho)}{\partial t} + \nabla \cdot (\rho \mathbf{u}) = 0, \quad (9)$$

$$\frac{\partial(\rho \mathbf{u})}{\partial t} + \rho \mathbf{u} \cdot \nabla \mathbf{u} = -\nabla P + \nabla \cdot (2 \mu \mathbf{S}_{ij}) + \nabla \cdot (-\rho \overline{u' u'}) + \nabla \cdot (2 \overline{\mu' S'_{ij}}) \quad (10)$$

$$\mathbf{S}_{ij} = \frac{1}{2} [\nabla \mathbf{u} + (\nabla \mathbf{u})^T] \text{ and } \mathbf{S}'_{ij} = \frac{1}{2} [\nabla \mathbf{u}' + (\nabla \mathbf{u}')^T] \quad (11)$$

$$\frac{\partial(\rho k)}{\partial t} + \frac{\partial}{\partial x_j} (\rho k u_j) = \frac{\partial}{\partial x_j} \left[\left(\mu + \frac{\mu_t}{\sigma_k} \right) \frac{\partial(k)}{\partial x_j} \right] + G_t - \rho \varepsilon \quad (12)$$

$$\frac{\partial(\rho \varepsilon)}{\partial t} + \frac{\partial}{\partial x_j} (\rho \varepsilon u_j) = \frac{\partial}{\partial x_j} \left[\left(\mu + \frac{\mu_t}{\sigma_\varepsilon} \right) \frac{\partial(\varepsilon)}{\partial x_j} \right] + C_1 \frac{\varepsilon}{k} G_t - C_2 \rho \frac{\varepsilon^2}{k} \quad (13)$$

$$G_t = (-\rho \overline{u'_i u'_j}) \cdot \nabla \mathbf{u} = \left(2 \mu_t \mathbf{S}'_{ij} - \frac{2}{3} \rho k \delta_{ij} \right) \cdot \nabla \mathbf{u} \quad (14)$$

$$T = \max\left(\frac{k}{\varepsilon}, C_t \sqrt{\frac{\nu}{\varepsilon}}\right), C_t = 1 \quad (15)$$

In the RANS framework, the mean values of field variables are solved and information about fluctuation components are lost. One such quantity is the shear rate, which has special importance for the calculation of viscosity in the HB model. In the shear-rate correction method of Gavrilov and Rudyak [9], the fluctuation component of the shear rate tensor is recovered by an approximation. This approximation, i.e., $\rho\varepsilon = \mu \overline{2S_{ij}'S_{ij}'}$, is in accord with the definition of the isotropic dissipation rate introduced by Tennekes and Lumley [16] and relates the mean dissipation rate of turbulence (ε) to the fluctuation component of the shear rate. Consequently, modified expressions for the shear rate and its extension to the HB model are obtained, as shown by Eq. (16) and Eq. (17), respectively.

$$|\Upsilon|_{\text{SRC}}^2 = 2 S_{ij}S_{ij} + \frac{\overline{2S_{ij}'S_{ij}'}}{2S_{ij}S_{ij}} = 2 S_{ij}S_{ij} + \frac{\varepsilon\rho}{\mu_{\text{H-BSRC}}} \quad (16)$$

$$\mu_{\text{H-BSRC}} = \frac{|\tau|}{\Upsilon_{\text{SRC}}} = \frac{\tau_Y}{\Upsilon_{\text{SRC}}} + k \Upsilon_{\text{SRC}}^{(n-1)} \quad (17)$$

In the above equations, Υ and ν are shear rate and the kinematic viscosity, respectively, and the subscript ‘‘SRC’’ refers to shear rate correction approach of Gavrilov and Rudyak [9]. It is reminded that the value of $\mu_{\text{H-BSRC}}$ can be set to a constant, e.g., 8.8×10^{-4} Pa.s, in the first iteration of the numerical simulation. In the present work, application of the alpha method (direct viscosity correction) and the shear rate correction is investigated in the numerical simulation of a pipe flow that is explained hereafter.

4. Simulation Methodology

Flow of 1.5 wt% Laponite-based simulant inside a pipe was considered. Experimental and computational investigations of this flow in different regimes, i.e., laminar, transitional, and turbulent, were performed by Escudier and Presti [6] and Peltier et al. [13], respectively. Fig. 3 shows the axisymmetric computational domain which contains 2117 cells (almost 100×21) along with the line probe used for measurements. This grid is very similar to the grid used by Peltier et al. [13] in their simulations. We used finer grids containing 7328 ($\sim 198 \times 37$), 20447 ($\sim 393 \times 52$), and 28615 ($\sim 432 \times 66$) cells for grid-independence tests in places where finer grids were needed for a converged solution. Boundary conditions, as well as dimensions of the domain and properties of the fluid, are illustrated in Table 1. In addition, parameters used in mesh generation are listed in Table 2.

[Place Fig. 3 here.]

[Place Table 1 here.]

[Place Table 2 here.]

According to the proposed algorithm above, the simulation was initialized with a constant viscosity of 8.8×10^{-4} Pa.s (for water in standard condition) and in the second iteration the field function for the proposed viscosity model, i.e., Eq. (8), and the SRC method, i.e., Eq. (17), were introduced to the Star-CCM+. Profile of viscosity and axial viscosity were obtained at the location $x=0.98L$, where L is the length of the periodic pipe. Small changes of the mean quantities, e.g., axial velocity on the line probe and domain-averaged viscosity, were our criteria for the system to reach a steady state condition. Data associated with field variables, such as axial velocity, wall-averaged viscosity, and shear rate at wall were reported once the mean values of criteria did not change with more iterations.

To study the computational error, we calculated the average of relative error between the experimental and numerical profiles in each simulation case. A first order interpolation scheme was used to locate each experimental data point between two consecutive points on any numerical profile that was under investigation. The relative error between corresponding experimental and numerical values was found and an array of error values was constructed from all corresponding points for each simulation case. Later, this error-array was averaged according to Eq. (18) in order to obtain a percentage error for each simulation case. In this expression, λ and N are the index and the total number of experimental data points for each simulation case, respectively.

$$\text{Err}_{\text{avg.}} (\%) = \frac{100}{N} \times \sum_{\lambda=1}^N (|f_{\text{exp}}(\lambda) - f_{\text{sim}}(\lambda)|) / f_{\text{exp}}(\lambda) \quad (18)$$

Later, we compared the error values obtained from the core method, i.e., the HB method, with other derived methods. This comparison, as shown by Eq.(19), was introduced in form of improvement of average percentage error for each method and helped us to quantify the contribution of different methods in improving the HB method.

$$\text{Err}_{\text{imp.}} (\%) = 100 \times \frac{|(\text{Err}_{\text{avg.}})_{\text{models}} - (\text{Err}_{\text{avg.}})_{\text{HB}}|}{(\text{Err}_{\text{avg.}})_{\text{HB}}} \quad (19)$$

5. Simulation results

HB, SRC, and Direct-Alpha models were implemented in simulations with various Reynolds numbers and grid spacing levels. The purpose of this study was to ensure grid-independency of result for each model and to obtain results

useful for further comparisons. In each effort, the simulation was started with a 2117-cell grid until a steady state condition was obtained, i.e., the mean of variables did not change with time any further. Later, the process was repeated with a 7328-cell grid, and in cases that results deviated from the 2117-cell case by more than one percent, finer grids with 20447, or in rare cases 28615 cells, were used. This checking procedure was continued to obtain unchanging results with regards to the grid spacing. Results of this study are illustrated in **Fig. 4** for all models and Reynolds number.

In the case of the laminar flow, turbulent solver was mistakenly used for the HB model leading to an interesting result. It is observed that the HB method produced almost identical results with both laminar and turbulent solvers, as shown in **Fig. 4**. The distinction between turbulent and laminar solvers is made clearly for each plot using the appropriate legend name. This result motivated the author to use the SRC and Direct-Alpha models for the laminar flow. Therefore, a set of additional plots is displayed for all simulations in laminar regime. Other plots in Figs. 4-7 show that there are slight changes of simulation results with significant increase of grid resolution for all Reynolds numbers and viscosity models.

[Place Fig. 4 here.]

5.1. Direct-Alpha method

The grid-independent results along with the experimental data points are included in **Fig. 5** and **Fig. 6**. Results for the laminar flow are separately shown in **Fig. 5** for better comparisons. **Fig. 6** shows results for both transitional and turbulent flow cases.

[Place Fig. 5 here.]

[Place Fig. 6 here.]

Results for the laminar flow simulated with both laminar and k- ϵ solvers, the HB method produced almost identical results, as shown in **Fig. 5(a)**. In addition, only a slight difference, almost one percent, exists between profiles obtained by SRC and other models. For this reason, the SRC model is not included in the **Fig. 5(b)**. Similarly, in **Fig. 5(b)**, difference between laminar and turbulent solvers 1.3 percent for the Local-Alpha method. This difference was 1.9 percent in $r/R = [0 \text{ to } 1]$ and 9 percent in $r/R = [0 \text{ to } 0.3]$ for the Global-Alpha method. In overall, predictions obtained by the Global- and Local-Alpha methods, are not better than those obtained by the HB method. Increase in the total error calculated by Eq. 19 is 46 percent by the Global-Alpha method and 61 percent by the Local-Alpha methods. However, similarity is observed between the profiles obtained by the HB and Local-Alpha methods, which indicates smaller effects of local adjustments in comparison to global adjustments of the viscosity. A 95 percent increase of error is observed due to global adjustment of viscosity in the core flow region, i.e., $r/R = [0 \text{ to } 0.6]$. In this region, adjustment of viscosity to a

significantly small value (compared to the HB viscosity values) resulted in significant over-prediction of shear rate and consequently the velocity. Here, large variations are attributed to the dramatic influence of the viscosity in the flow field, which is the nature of flows in laminar regime.

For the transitional flow case ($Re = 3400$), as **Fig. 6(a)** shows, the prediction obtained by the Global-Alpha method is significantly better than the original HB method. Improvements are observed almost over the entire length of the probe, where error is reduced by 48% in comparison to the HB method. These improvements are more pronounced in the core flow region, i.e., $r/R = [0 \text{ to } 0.55]$, where a 73% reduction of error happened in comparison to the HB method. Unlike this non-flat profile, the HB and shear correction (SRC) methods, predicted similar flat profiles with only 1.3% of difference in the same region. The error with these flat profiles is almost 8% and flatness of the profiles is an indication of zero shear stress in this region. On the lower half length of the probe, i.e., $r/R = [0.55 \text{ to } 1]$, deviation from the experimental values is almost 51% for the HB and SRC methods versus 29% for the Global-Alpha method. Unlike the Global-Alpha method, the Local-Alpha method has produced similar results to the HB method and maximum difference between these models is only 4.2%.

For the turbulent flow ($Re = 25300$), as **Fig. 6(b)** shows, all models predicted the velocity profile accurately in the near wall region, i.e., in $r/R = [0.9 \text{ to } 1]$. In this region, implementation of the Global-Alpha has resulted in 2% error improvement. In the median region, i.e., in $r/R = [0.45 \text{ to } 0.9]$, a maximum of 3% difference is observed between the results of the HB, SRC, and Local-Alpha methods; however, implementation of the Global-Alpha method has resulted in lower velocity magnitudes, which better agrees with the experimental data, with a 45% reduction of error, in comparison to the HB method. In the core flow region, i.e., in $r/R = [0 \text{ to } 0.45]$, all methods have over-predicted the velocity values. Flat profiles are observed for the HB and SRC methods in the core flow region $r/R = [0 \text{ to } 0.4]$, unlike the Global-Alpha method, which predicted a continuous trend of increase of axial velocity. Thus, the shear rate predicted by the Global-Alpha method is in better agreement with the shear rate of the experiment. In addition, implementation of the Global-Alpha has resulted in 0.7% increase of accuracy in comparison to the HB method.

Further, we extended our investigation to the analysis of the viscosity calculation along the line probe. The purpose of this investigation was to better understand the differences observed earlier regarding the profiles of velocities predicted by different models. For this purpose, we included the profiles obtained from the HB and SRC, along with the effective version of the alpha-method, i.e., the Global-Alpha method. **Fig. 7** shows the variation of viscosity along the probe line for the three flow regimes under investigation in this study. For each regime, the viscosity obtained from the Direct-Alpha method, also called as α -viscosity, is shown in red dots and is a constant value. This scalar is multiple orders of magnitude smaller than the viscosity values predicted in the flow core region by HB and SCR methods.

[Place Fig. 7(a) here.]

[Place Fig. 7(b) here.]

[Place Fig. 7(c) here.]

Fig. 7 shows a descending trend of the α -viscosity with increasing Reynolds number. This trend is in accord with significantly higher shear rates at the wall region for a turbulent flow in comparison to a laminar flow. In addition, all the plots display a sudden increase of the viscosity by increase of the distance from the wall, i.e., by approaching the core flow or center of the pipe. This sudden increase of the viscosity is delayed for the SRC method in the high Reynolds number, i.e., $Re = 25,300$. In fact, the HB model in its original form, i.e., in $\mu = \tau_y / \dot{\gamma} + k\dot{\gamma}^{(n-1)}$, is subject to singularity in the core flow region, where the shear rate approaches zero. This singularity can be seen in **Fig. 7** by sudden escalation of shear stress in all flow regimes.

In the laminar flow with $Re = 550$, as shown in **Fig. 7(a)**, an increase of the HB viscosity to the α -viscosity is observed in the wall region indicated as “region of increased viscosity” on the plot. This increase of viscosity happened in $y/R = [0 \text{ to } 0.24]$ for the laminar flow, where y represents distance from the wall. This region is relatively larger for the laminar flow in comparison to transitional and turbulent regimes, as will be explained later. This increase of the viscosity, which is 47% on average, is in accord with lower axial velocities obtained by the Global-Alpha method in comparison to the HB method, according to **Fig. 5(b)**. Beyond this point, this treatment has resulted in a continuous drop of viscosity from the HB level and consequently increases the shear rate and axial velocities as is seen in **Fig. 5(b)**.

The profile of viscosity for the transitional flow at $Re = 3400$ is shown in **Fig. 7(b)**. Our analysis reveals a 32 % increase of the viscosity in the wall region, i.e., $y/R = [0 \text{ to } 0.18]$, through implementation of the Global-Alpha method in comparison to the HB method. This increase of viscosity has resulted in better prediction of velocity profile in this region, as shown in **Fig. 5(b)**, and 43% smaller error in comparison to the HB method. Further away from the wall, i.e., $y/R = [0.45 \text{ to } 1]$, adjustment of viscosity by the Global-Alpha method has resulted in higher velocities, which better agreed with the experimental data, as shown in **Fig. 6(a)** and i.e., 73% improvement of error. One notable fact is that similar to the Global-Alpha method, implementation of the SCR method has resulted in significant reduction of the viscosity from the HB viscosity. On average, the reductions were 89% in $y/R = [0 \text{ to } 0.18]$, and almost a 100% in $y/R = [0.45 \text{ to } 1]$. However, despite these significance differences, only a 1.3% difference is observed between the velocity profiles obtained from HB and SRC methods, according to **Fig. 6(a)**

5.2. In the case of the turbulent flow, i.e., $Re = 25,300$, similar values of viscosity are obtained from all the models near the wall in Fig. 7(c), i.e., in $y/R = [0 \text{ to } 0.2]$. This explains why small differences are observed between velocity profiles in Fig. 5(a). In this regime, the increase of viscosity is observed in a very small region in the vicinity of the wall, i.e., i.e., $y/R = [0 \text{ to } 0.02]$. On the other hand, Fig. 7(c) shows that large deviations between

viscosity profiles occurs in regions away from the solid boundary, i.e., in $y/R = [0.4 \text{ to } 1]$. In the median range of, i.e., $y/R = [0.1 \text{ to } 0.55]$, the average of deviations between the HB and SRC's viscosity profiles is about 30%. However, deviation between velocity profiles of these models shown in Fig. 6(b) is only about 3%. Similarly, deviation between viscosity profiles is about 99.2% on average in the core flow region, i.e., $y/R = [0.55 \text{ to } 1]$ in Fig. 7(c), while velocity profiles of HB and SRC depart by less than 4% in Fig. 6(b). This behavior can be associated with weakened action of the viscosity in comparison to the inertia effects in the core flow regions of turbulent flows. **Inverse-Alpha Method**

Earlier in this paper, it was shown that utilization of a small value of viscosity could dramatically alter the simulation results. Special attention was given to the turbulent and transitional flows since improvement of the velocity profile was observed approximately over the entire length of the probe. In order to investigate the effect of further reduction of the viscosity, a substitute viscosity with a smaller value compared to the Eq. (8) can be used. Thus a new method, named as the Inverse-Alpha method, is introduced. In this method, a reduced substitute viscosity in comparison to the direct alpha-method is used. The justification of the proposed concept is that in every iteration a smaller area under the straight line, i.e., pseudo-Newtonian line, will be considered rather than the area under the HB curve. Consequently, Eq. (8) transforms into Eq. (20) to represent the Inverse alpha-method.

$$\mu_{\text{alpha.inv.}} = \begin{cases} \mu_{\text{H-B}} = \frac{|\tau|}{Y} = \frac{\tau_Y}{Y} + k Y^{(n-1)} & \varepsilon_{\text{H-B}} \leq \varepsilon - \text{THS} \\ \frac{\mu_{\text{pseudo_Newt.}}}{\alpha} & \varepsilon_{\text{H-B}} > \varepsilon - \text{THS} \end{cases} \quad \text{Eq.(20)}$$

Here, the range for the non-linearity coefficient, i.e., $\alpha > 1.3$ guarantees smaller values of viscosity in comparison to Eq.(8).

To implement this method, we used the same algorithm that was introduced earlier for the Direct-Alpha method. Similar to the past, we applied this method to different grid size levels and regimes of the flow. **Fig. 8** shows the results of grid-independency study for the versions of the Inverse-Alpha viscosity model. These results show only slight differences between results obtained on fine and course meshes.

[Place Fig. 8 here.]

Grid-independent results from the Inverse- and Direct-Alpha models are compared in **Fig. 9** and **Fig. 10** for different Reynolds numbers. A quantitative comparison of error values and error improvements for different models and

Reynolds number is also provided in **Table 3** and 4. **Fig. 9** shows the results obtained from the laminar flow using both the laminar and k- ϵ solvers and different behavior are observed. In local adjustment of viscosity, as shown in **Fig. 9(a)**, modeling is insensitive to the solver but insensitive to the viscosity model (direct or inverse). In contrary, In global adjustment of viscosity, as shown in **Fig. 9(b)**, modeling is sensitive to the solver but insensitive to the viscosity model. The best combination, i.e., Inverse Global-Alpha model and the k- ϵ turbulence model has resulted in significant improvement of error over the entire length of probe, which was almost 81 percent.

For the transitional flow with $Re = 3400$, the largest error reduction (48 percent) is obtained using the Global-Alpha method (direct form) as shown in **Fig. 10(a)**. Performance of this model is significantly better in comparison to all other models shown in this figure. In addition, no credible improvement is observed by using the Inverse Local-Alpha model in both direct and inverse forms.

For the turbulent flow case, profiles obtained from the Global and Inverse Global-Alpha methods are in good agreement with the experimental data as shown in **Fig. 10(b)**. Improvements are 48 and 61 percent reduction of relative error, respectively. Here, the inverse and global adjustments of viscosity together have resulted in improvement of the profile over the entire length of the probe.

[Place Fig. 9 here.]

[Place Fig. 10 here.]

[Place Table. 3 here.]

[Place Table. 4 here.]

In addition, turbulent velocity profiles ($U^+ = U/U^*$) represented in wall variables ($Y^+ = \rho Y U / \mu_{\text{wall}}$) were obtained for all the models used in this paper. U^* is the wall friction velocity and was calculated as $U^* = (\tau_{\text{wall}} / \rho)^{1/2}$, where τ_{wall} and μ_{wall} are the viscosity and shear stress at the wall. Qualitatively (**Fig. 11** and **Fig. 12**) and quantitative (**Table 5** and **Table 6**) comparisons with associated experimental values (reported by Escudier and Presti [21]) were also made. These tables show different numbers of data points for comparison since different ranges of Y^+ were reported by the simulations. Therefore, comparisons use: (1) available simulation data points, and (2) maximum data point reported among all methods. The second comparison was made to compare the capability of modeling in representing the U^+ over the entire range of Y^+ reported by Escudier and Presti [21]. In error calculation, we looked for simulation data points around each experimental data point. Early termination of some numerical profiles, e.g., **Fig. 12(a)** at Y^+ of 370, have left some experimental data points without associated numerical data points which are called here as orphan points. An error value of 100% has been assumed for all orphan points in all plots. This error study was further extended to two distinct

ranges of Y^+ for each flow case, i.e., $0 \leq Y^+ \leq 20$ and $20 < Y^+ \leq 1000$ for $Re = 3400$, and $0 \leq Y^+ \leq 40$ and $40 < Y^+ \leq 1000$ for $Re = 25300$. In the first range, which contains low Y^+ values, profiles follow the experimental values closely and this range has not been much of attention for comparison of accuracy. For this reason, the low- Y^+ value regions are not included in **Table 5** and **Table 6**. In contrary, the difference between numerical and experimental profiles is significantly larger in the second range, which contains larger values of Y^+ .

[Place Fig. 11 here.]

[Place Fig. 12 here.]

For the transitional flow case, all profiles agree closely with the experimental values up to Y^+ of 20, except for the Local_alpha method. This method, along with the original HB and SRC methods, has resulted in an even earlier flattening of the U^+ profile. Such a trend is observed comparably very later for the Inverse Local-Alpha method and is absent for the Global-Alpha method, the Inverse Global-Alpha method, and the experimental data. In addition, **Fig. 11** shows extension of predictions to the entire range of Y^+ values through the use of Inverse Alpha methods (both Local and Global schemes). Comparison of error values in Tables 5 in $0 \leq Y^+ \leq 1000$ and $20 < Y^+ \leq 1000$ indicates that the smallest average error occurs when using the Inverse Local-Alpha method. This held true with both inclusion and exclusion of orphan points. However, even though the Inverse Local-Alpha method demonstrated a poor performance when the mean velocity profile (U) is considered, according to **Fig. 10(a)**, **Table 3**, and **Table 4**. Rather, the Global-Alpha method is rated the best according to Table 3 and Table 4. Table 5 shows that use of the Global-Alpha method significantly increases the error in both $0 \leq Y^+ \leq 1000$ and $20 < Y^+ \leq 1000$ ranges if orphan points are considered.

The key to understanding this discrepancy is taking into account the significant deviation of the experimental U^+ values from a typical log-law profile, as was represented by Escudier and Presti [21] for $Re = 3400^\dagger$. On the contrary, the global alpha method (both in direct and inverse forms) results in a typical log-law relationship at high Y^+ values due to use of a pseudo-Newtonian viscosity. Therefore, local adjustment of viscosity could have better represented the aforementioned deviation and resulted in better prediction of the U^+ values.

For the turbulent flow case, **Fig. 12** shows that all profiles agree closely with the experimental values up to Y^+ of 40. Flattening of profiles occurred similar to the transitional case with some differences for the SRC method. Here, the agreement between data points in the case of the Global and Inverse Global-Alpha methods (plots d and f) are exceptional. Similar to the transitional flow simulations, the use of the inverse and global forms resulted in extension of

[†] Escudier and Presti [21] reported a different pattern for the turbulent flow case, where experimental U^+ values closely followed a typical log-law profile.

predictions to almost entire range of Y^+ values. Comparison of error values in **Table 6** in $0 \leq Y^+ \leq 1000$ (when considering orphan points) and $40 < Y^+ \leq 1000$ (with both inclusion and exclusion of orphan points) indicates that the smallest average error occurred when using the Inverse Global-Alpha method. Interestingly, using the Inverse Global-Alpha method was also rated the best method version for the fully turbulent case when regarding the mean velocity profile (U) instead of the U^+ . Therefore, this model version could best represent the flow characteristics of the fully turbulent case.

[Place Table. 5 here.]

[Place Table. 6 here.]

Summary and Concluding Remarks

In this paper, we presented a method to obtain and utilize alternative viscosity values during RANS simulations for non-Newtonian flow in a pipe. This method was used to reduce the magnitude of the viscosity that was obtained by the HB model in a large portion of the domain in all of the simulation cases tested. In all regimes of the flow, the alpha-method worked to increase the viscosity in small portions of the computational domain. This effect weakened with the increase of the Reynolds number of the flow. Application of the Alpha method demonstrated significant potentials in improving the prediction of turbulent velocity profiles represented by both mean (U) and wall variable (U^+) forms as compared to the results obtained from the original HB method.

Applications of the HB and shear correction method of Gavrilov and Rudyak [9] for simulation of laminar and transitional flow cases tested in this paper were accompanied by significant computational errors. These models produced almost identical results, although they generated significantly different magnitudes for the viscosity.

Considering the Direct-Alpha method and focusing on the U values, global adjustment of viscosity resulted in 48 and 26 percent improvements of velocity profiles for the transitional and turbulent flow cases, respectively. No improvement was observed by using the Global-Alpha method for simulation of the laminar flow. Interestingly, no difference was observed between simulation results using the laminar and turbulent solvers. For the Local-alpha method, no improvements were observed for all the regimes considered.

Considering the Inverse-Alpha method and focusing on the U values, global adjustment of viscosity resulted in 81 and 61 percent improvements of velocity profiles for the laminar and turbulent cases, respectively. Improvement in the laminar case was obtained once the flow was simulated using the turbulence solver. No improvement was observed by using the Inverse Alpha methods (with Local or Global version) for simulation of the laminar flow.

Considering the U^+ values, application of the Alpha method in its inverse form was the most effective approach to obtain improvements. Reduction of deviations from experimental U^+ values as well as extension of predictions to full range of Y^+ were used as criteria for improvements. Implementation of the Inverse Local- and Inverse Global-Alpha methods resulted in 53 percent and 76 percent error reductions, respectively.

By considering the improvements on both U and U^+ profiles for the flow cases in this paper, it is concluded that the Inverse Global-Alpha method has significant potentials to be used for simulation of fully turbulent flows of viscoplastic materials. This method showed potentials for simulation of Laminar flows. However, no conclusion could be made regarding an appropriate model version for simulation of transitional flows. Future investigations can focus on different fluid properties and boundary conditions.

Acknowledgments

Funding for this work was provided by the Department of Energy's National Energy Technology Laboratory under grant number DE-FE0007260.

References

- [1] Andrade L.C.F., Petronílio J.A., de A. Maneschy C.E., de A. Cruz D.O., 2007, The Carreau-Yasuda Fluids: a Skin Friction Equation for Turbulent Flow in Pipes and Kolmogorov Dissipative Scales, *Journal of the Brazilian Society of Mechanical Science and Engineering*, Vol. 29, Issue 2, p163
- [2] Bartosik A., 2010, Application of Rheological Models in Prediction of Turbulent Slurry Flow, *Flow Turbulence, and Combustion*, Volume 84, pp 277–293
- [3] Bingham E.C., *Fluidity and Plasticity*, McGRAW-Hill Inc., 1922
- [4] Cross M.M., 1965, Rheology of non-Newtonian fluids: A New Flow Equation for Pseudoplastic Systems, *Journal of Colloid Science*, pp 417-437
- [5] Dodge D.w., Metzner A.B., 1959, Turbulent Flow of Non-Newtonian Systems, *AIChE journal*, Volume 5, Issue 2, p189
- [6] Escudier M.P., Presti F., 1996, Pipe Flow of a Thixotropic Liquid, *J. Non-Newtonian Fluid Mech.*, volume 62, PP. 291-306
- [7] Escudier M.P., Poole R.J., Presti F., Dales C., Nouar C., Desaubry C., Graham L., Pullum L., 2005, Observations of symmetrical flow behaviour in transitional pipe flow of yield-stress and other shear-thinning liquids, *J. Non-Newtonian Fluid Mech.* 127 (2005) 143–155
- [8] Gokaltun S., McDaniel D. and Roelant D., 2012, Three-dimensional Simulations of Multiphase Flows Using a Lattice Boltzmann Method Suitable for High Density Ratios, *WM2012 Conference*, February 26- March 1 2012,

Phoenix, AZ

- [9] Gavrilov A.A., Rudyak V.Y., 2014, A Model of Averaged Molecular Viscosity for Turbulent Flow of Non-Newtonian Fluids, Journal of Siberian Federal University, Journal of Mathematics & Physics, Volume 7, Issue 1, pp 46–57
- [10] Herschel W.H., Bulkley R., 1926, Kolloid-Zeitschrift, Volume 39, Issue 4, pp 291–300, doi:10.1007/BF01432034
- [11] Meyer P.A., Kurath D.E., Stewart C.W., 2005, Overview of the Pulse Jet Mixer Non-Newtonian Scaled Test Program, PNWD-3677, WTP-RPT-127 Rev. 0
- [12] Poloski A., Smith H., Smith G., Calloway T., 2004, Technical Basis for HLW Vitrification Stream Physical and Rheological Property Bounding Conditions. WTP-RPT-100 Rev. 0, Battelle – Pacific Northwest Division, Richland, Washington.
- [13] Peltier J, Andri R, Rosendall, Inkson N., Lo S., 2015, Evaluation of RANS Modeling of Non-Newtonian Bingham Fluids in the Turbulence Regime Using Star-CCM+®, Advanced Simulation & Analysis, BechtelNuclear, Security & Environmental, CD-adapco™, Conference: STAR Global Conference 2015.
- [14] Pinho F.T., Whitelaw J.H., 1990, Flow of Non-Newtonian Fluid in A Pipe, Journal of Non-Newtonian Fluid Mechanics, Volume 34, pp 129-144
- [15] Soto R.J., Shah V.L., 1976, Entrance Flow of a Yield-Power Law Fluid, Journal of Applied Science Research, Volume 32
- [16] Tennekes H., Lumley J.L., “A First Course in Turbulence”, The MIT Press, 1972, pp 64-66
- [17] Toms B.A., 1948, Some Observations on the Flow of Linear Polymer Solution through Straight Tubes at Large Reynolds Number, Proceedings of 1st Conference on Rheology, Vol.2, North Holland, Amsterdam, p135.
- [18] Thomas D.G., 1963a, Non-Newtonian Suspensions: Part 1, Physical Properties and Laminar Transport Characteristics, Industrial and Engineering Chemistry, pp 55-18
- [19] Thomas D.G., 1963a, Non-Newtonian Suspensions: Part 11, Turbulent Transport Characteristics, Industrial and Engineering Chemistry, pp 55-27
- [20] Wilson, K.C., Thomas A.D., 1985, A New Analysis of the Turbulent Flow of Non-Newtonian Fluids, The Canadian Journal of Chemical Engineering, Volume 63, pp 539-546
- [21] Escudier M.P., Presti F., 1996, Pipe Flow of a Thixotropic Liquid, J. Non-Newtonian Fluid Mech., volume 62, PP. 291-306.

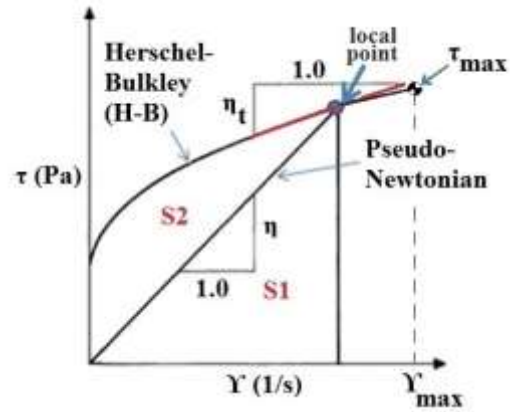


Fig. 1. Typical rheogram of a viscoplastic fluid.

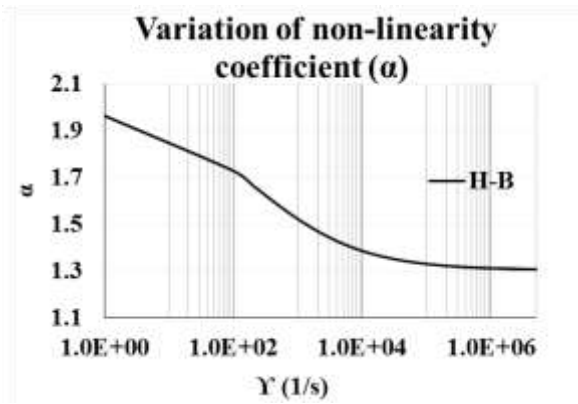


Fig. 2. Variation of stress-strain non-linearity (α) in a viscoplastic fluid.

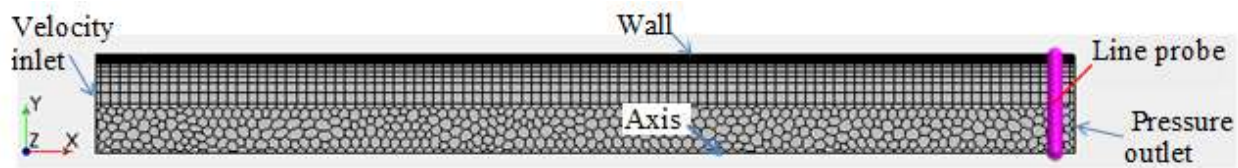
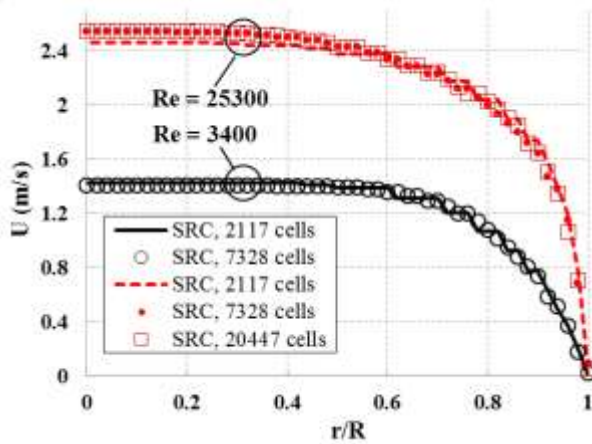
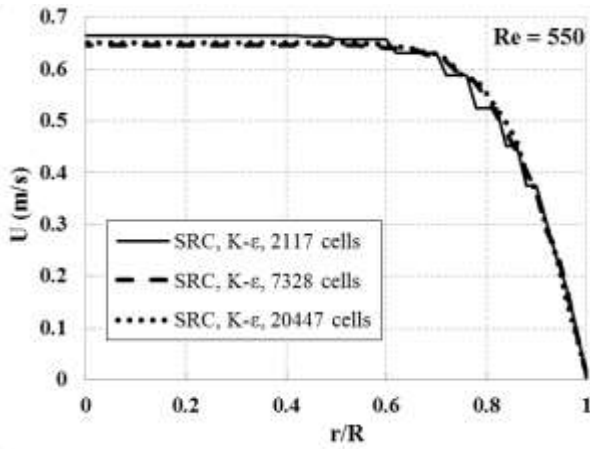
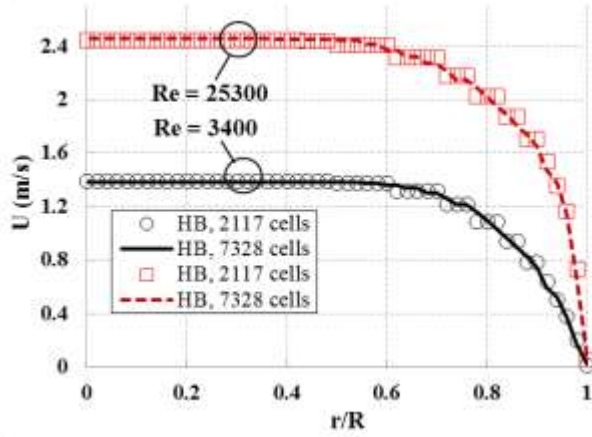
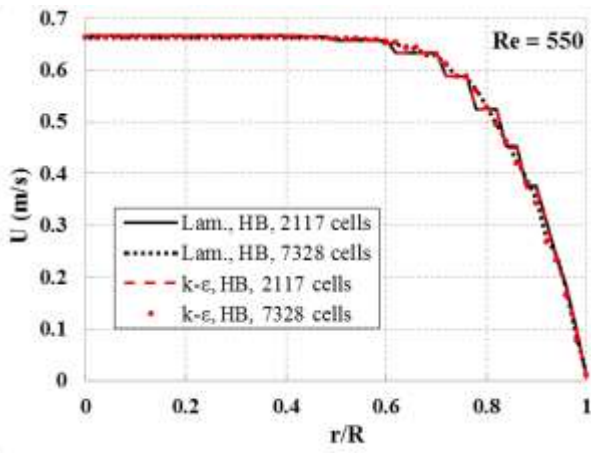


Fig. 3. Two-dimensional computational domain containing 2117 cells.



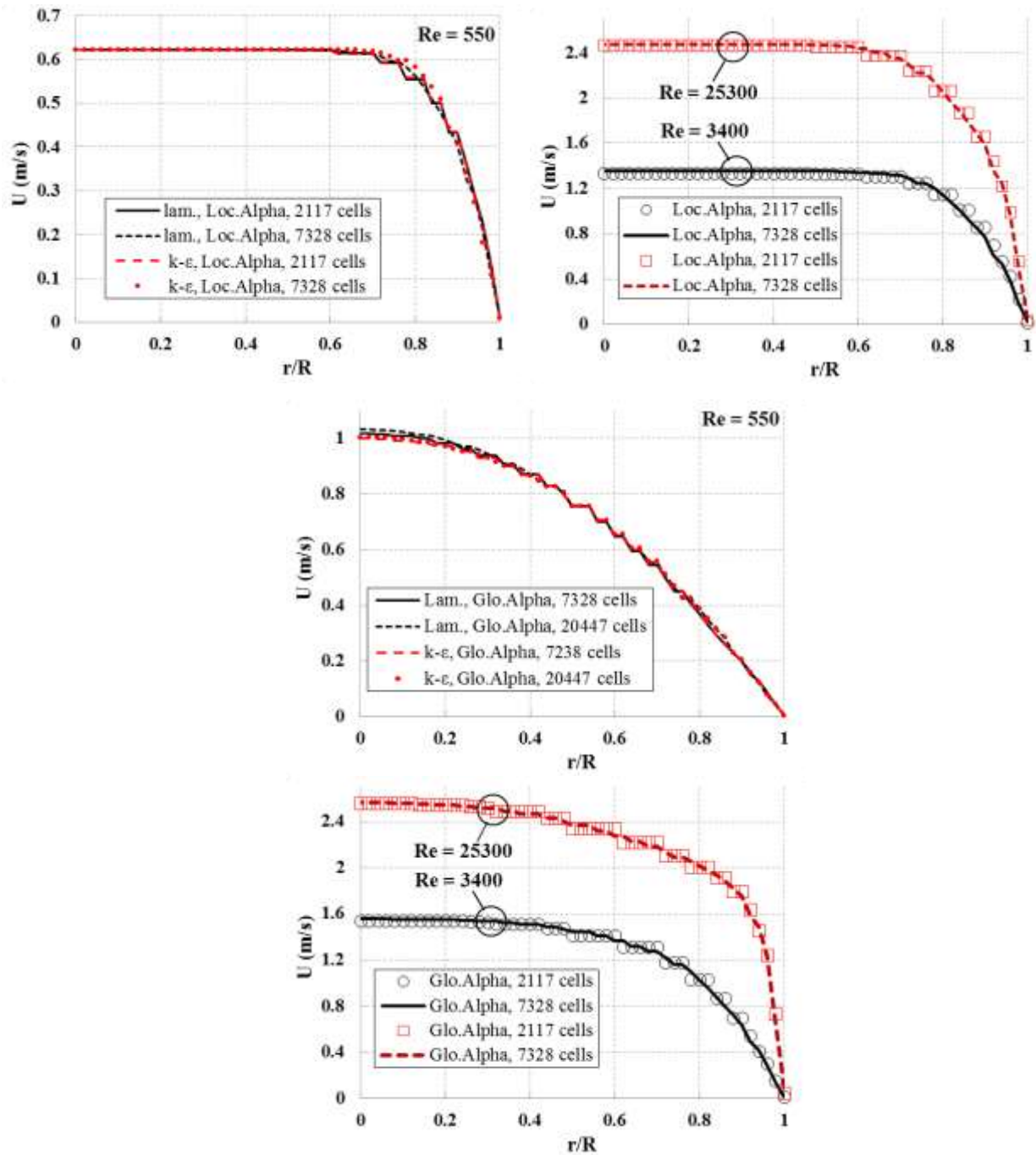


Fig. 4. Grid-independency study for the HB, SRC, and Direct-alpha viscosity model

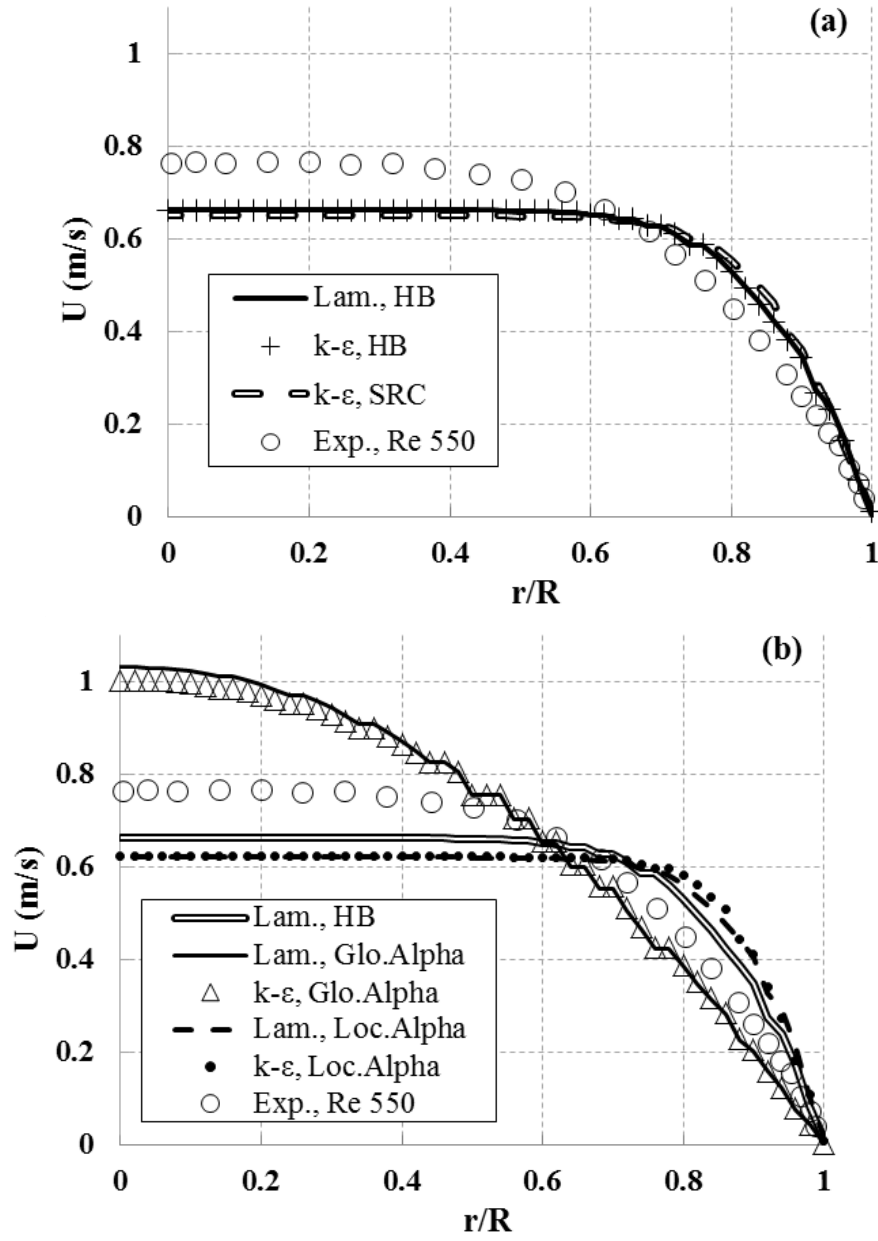


Fig. 5. Velocity profiles for the Direct-Alpha, HB, and SRC models, laminar flow.

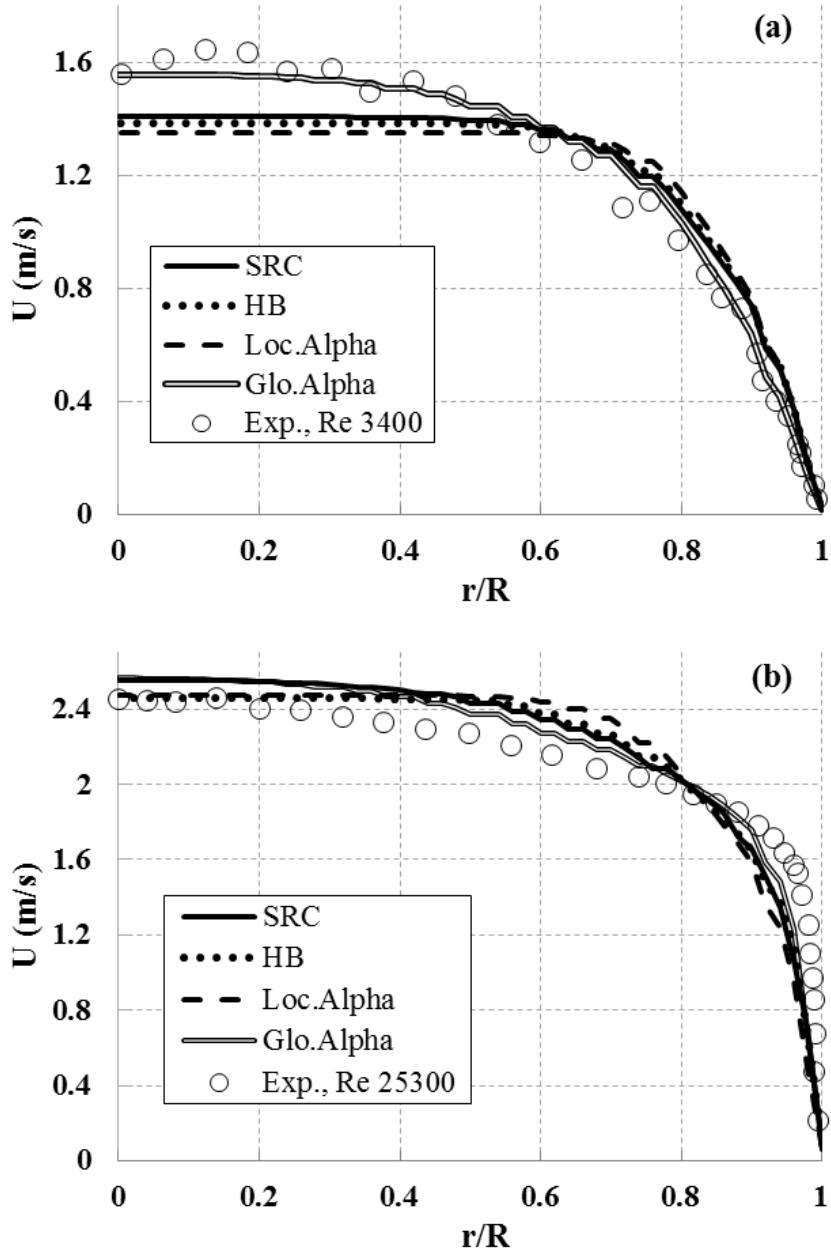


Fig. 6. Velocity profiles for the Direct-Alpha, HB, and SRC models, transitional and turbulent flows.

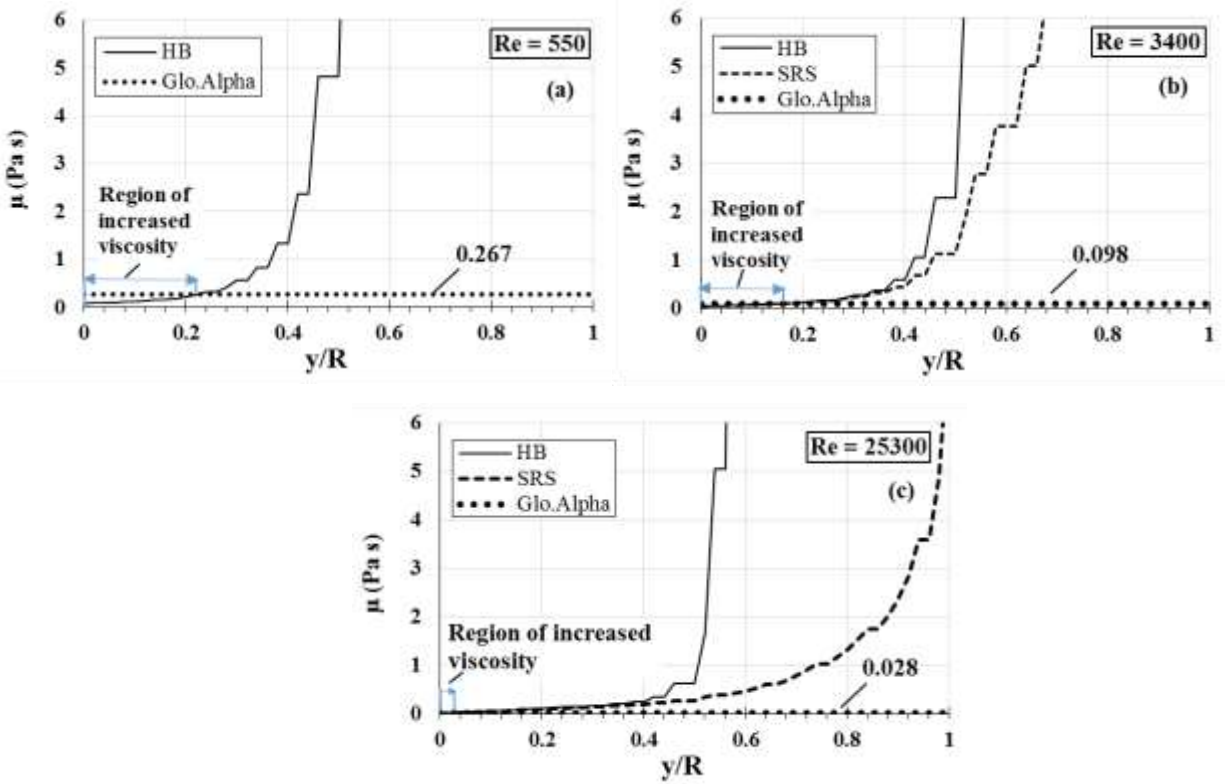


Fig. 7. Variation of viscosity in radial direction at $X=0.98L$ in different flow regimes.

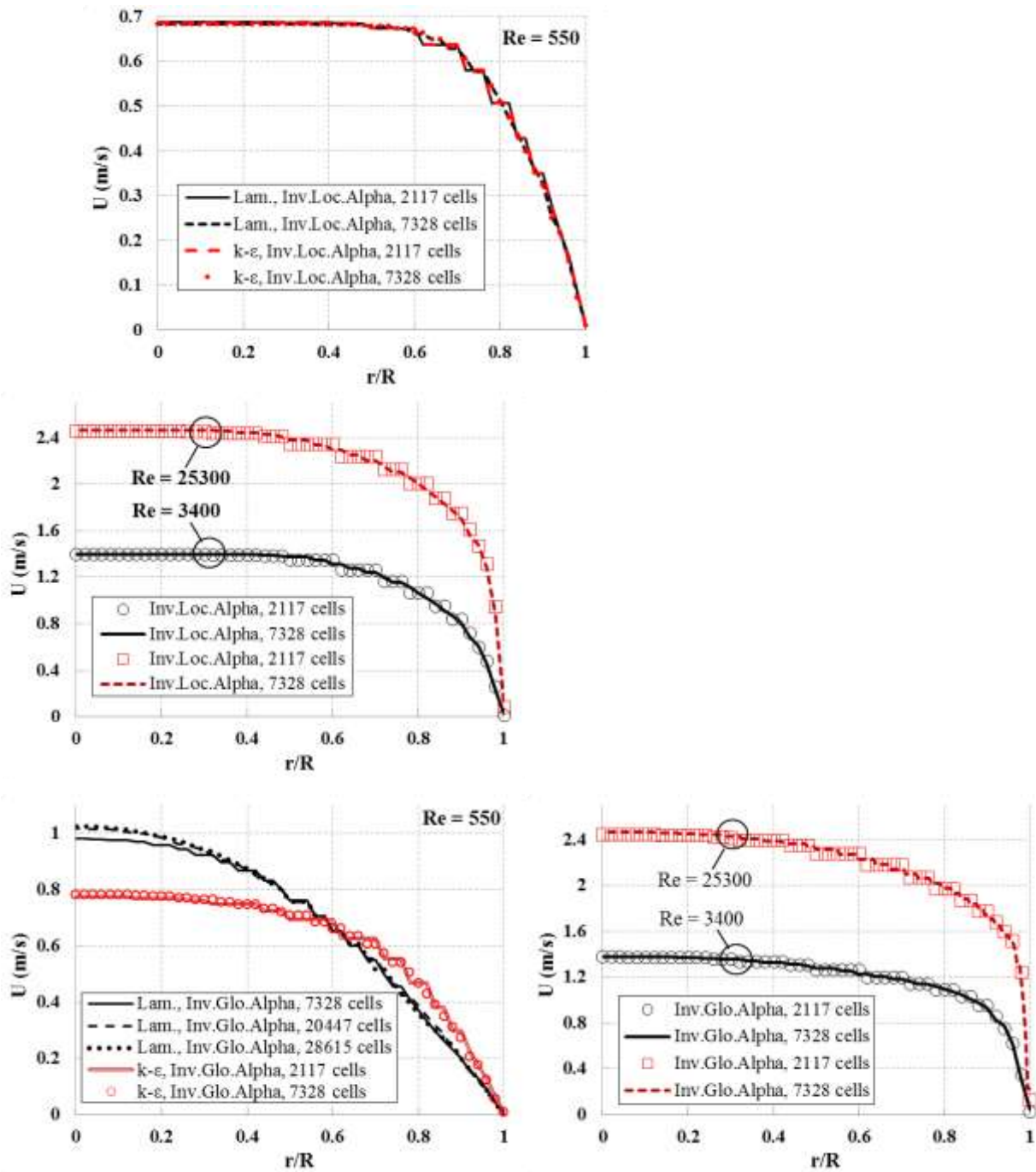


Fig. 8. Grid-independency study for the Inverse-alpha viscosity model.

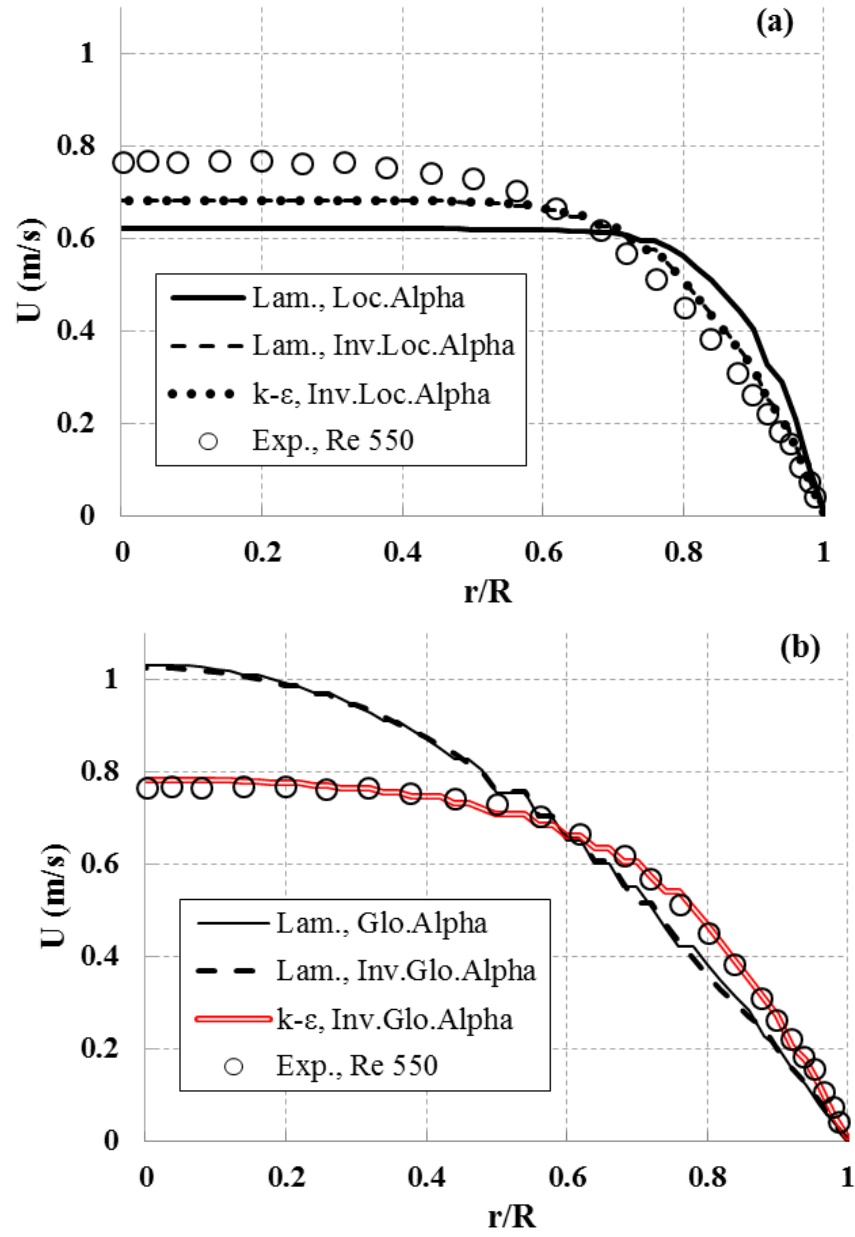


Fig. 9. Velocity profiles for the Inverse- and Direct-Alpha models, laminar flow.

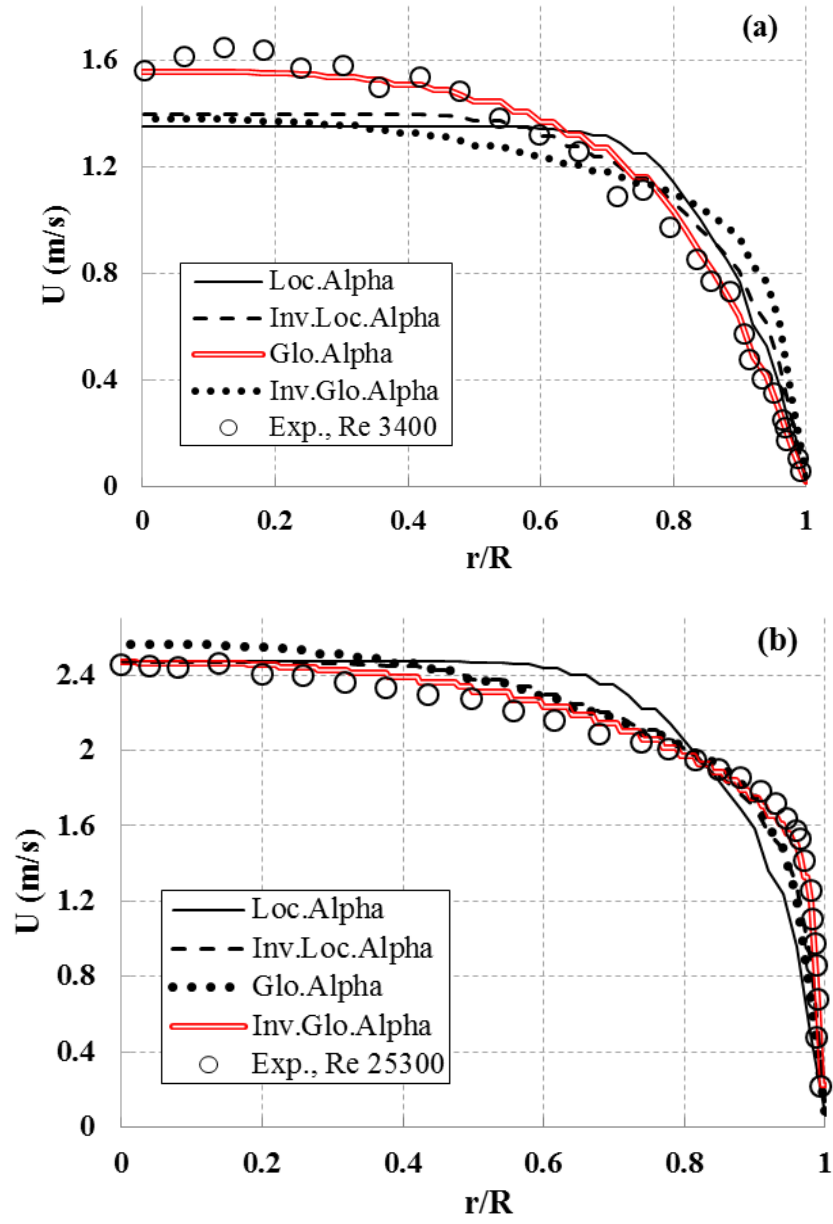


Fig. 10. Velocity profiles for the Inverse- and Direct-Alpha models, transitional and turbulent flows.

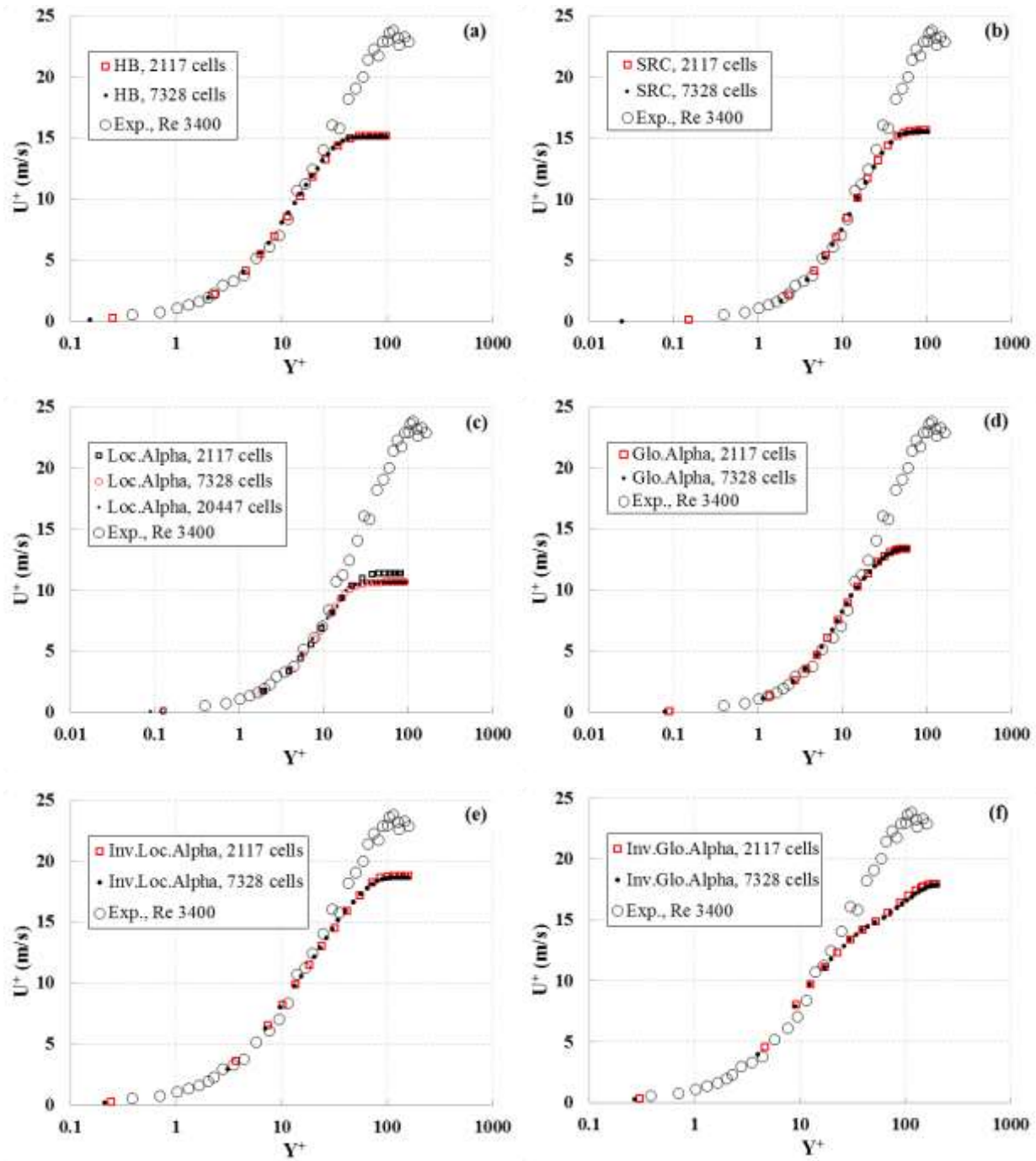


Fig. 11. Mean velocity profiles for the transitional flow in law-of-the wall coordinates.

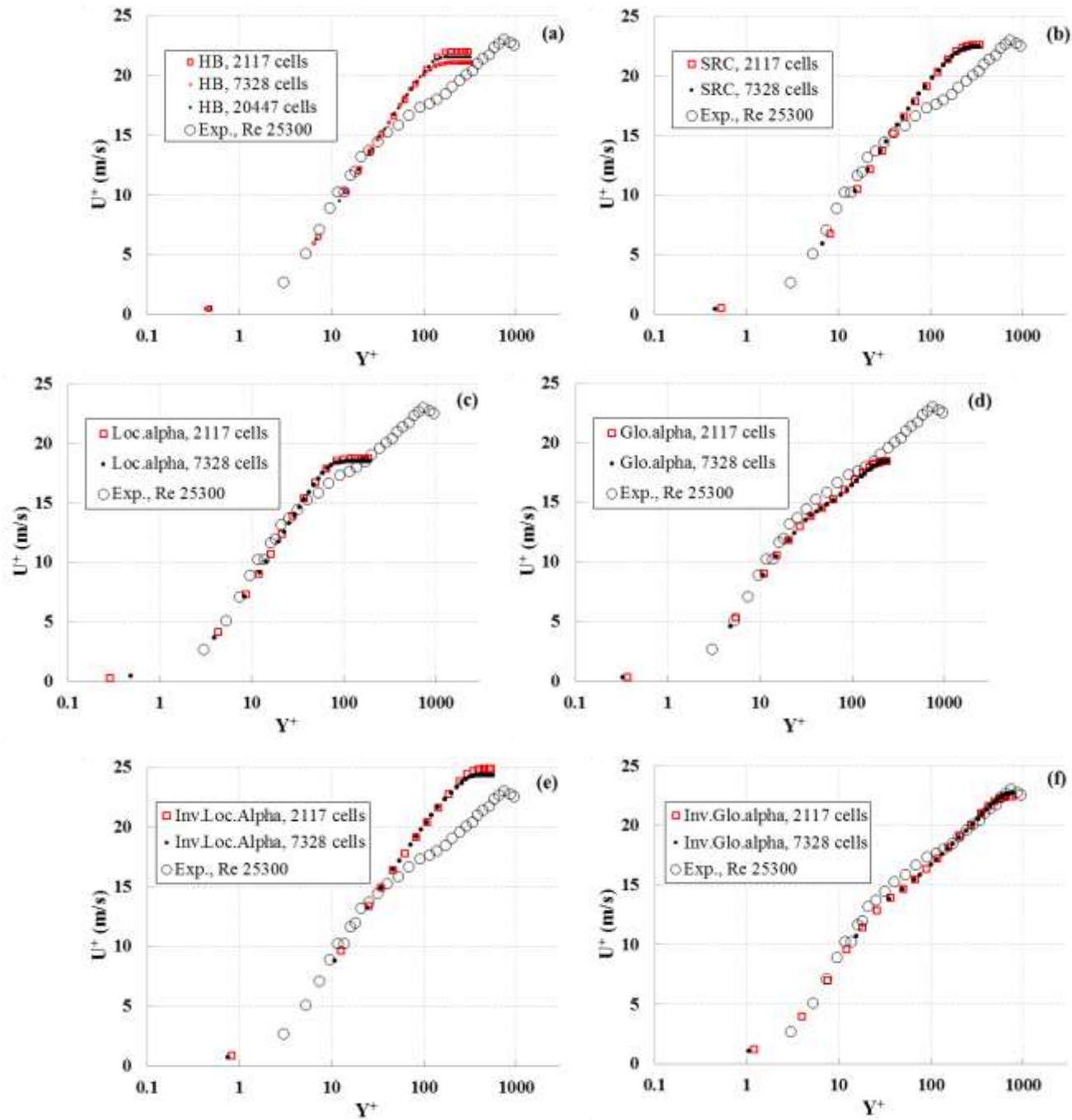


Fig. 12. Mean velocity profiles for the turbulent flow in law-of-the wall coordinates.

Table 1

Boundary conditions, geometry, and fluid properties in RANS simulations.

CASE	Re = 550	Re = 3400	Re = 25300
Boundary Conditions	Periodic	Periodic	Periodic
Inlet velocity, v_i (m/s)	0.52	1.09	2.03
Mass flow rate at interface, \dot{m} (kg/s)	4.08	8.56	15.94
Pressure at outlet	1atm	1atm	1atm
Fluid Properties	Domain and Mesh Dimensions		
Density, ρ (kg/m ³)	1000	Length (m)	0.5
Yield stress, τ_y (Pa)	4.42	Diameter (m)	0.1
Consistency factor, k (Pa s ⁿ)	0.242	Number of prism layer	20
Exponent, n	0.534	Grid	198×37, 393×52, 432×66

Table 2

Parameters for mesh generation

Parameters	Mesh 2117	Mesh 7328	Mesh 20447	Mesh 28615
Base size (m)	0.005	0.0025	0.00125	0.00105
Target size (m)	0.005	0.0025	0.00125	0.00105
Minimum surface size (m)	0.0005	0.00025	0.000125	0.000105
Surface curvature	36	36	36	36
Surface growth rate	1.3	1.001	1.001	1.001
# prism layer	15	25	25	40
Prism layer stretching factor	1.3	1.1	1.1	1.01
Prism layer total thickness (m)	0.025	0.025	0.025	0.025

Table 3

Error analysis study for different methods and flow regimes (see Eq.18).

Flow regime →	Laminar ^a (Re = 550)	Laminar ^b (Re = 550)	Transitions (Re = 3400)	Turbulent (Re = 25300)
Method ↓	Err _{avg.} (%)	Err _{avg.} (%)	Err _{avg.} (%)	Err _{avg.} (%)
HB	12.9	11.9	28.2	4.5
SRC	-	13.1	26.8	6.2
local_alpha	20.9	19.5	30.5	6.3
global_alpha	18.9	17.8	14.7	4.7
Inv._local_alpha	9.2	8.7	35.7	3.3
Inv._global_alpha	18.6	2.4	52.5	1.7

a: Solved by the laminar solver in STARCCM+

b: Solved by the k-ε solver in STARCCM+

Table 4

Improvement of percentage error for different methods and flow regimes (see Eq. 19)^a.

Flow regime →	Laminar ^a (Re = 550)	Laminar ^b (Re = 550)	Transitions (Re = 3400)	Turbulent (Re = 25300)
Method ↓	Err _{imp.} (%)	Err _{imp.} (%)	Err _{imp.} (%)	Err _{imp.} (%)
HB	N/A	N/A	N/A	N/A
SRC	N/A	-	-	-
local_alpha	-	-	-	-
global_alpha	-	-	48.1	26.2
Inv._local_alpha	28.6	33.1	-	-
Inv._global_alpha	-	81.4	-	61.4

N/A: not applicable - : no improvement (error increased)

a: Solved by the laminar solver in STARCCM+

b: Solved by the k-ε solver in STARCCM+

Table 5

Mean relative error for U+ values, (Re = 3400).

Method	$0 \leq Y^+ \leq 1000$ possible points		$0 \leq Y^+ \leq 1000$ Max. points (34 points)	$20 \leq Y^+ \leq 1000$ possible points		$20 \leq Y^+ \leq 1000$ Max. points (17 points)
	# of points	Erravg. (%)		# of points	Erravg. (%)	
HB	27	14.1	31.8	10	22.1	54.1
SRC	28	16.1	30.9	11	22.5	49.8
local_alpha	27	25.6	40.9	10	43.4	66.7
global_alpha	23	13.3	41.4	6	24.4	73.3
Inv._local_alpha	33	12.3	14.9	16	15.6	20.5
Inv._global_alpha	34	16.7	16.6	17	24.3	24.3

Table 6

Mean relative error for U+ values, (Re = 25300).

Method	$0 \leq Y^+ \leq 1000$ possible points		$0 \leq Y^+ \leq 1000$ Max. points (34 points)	$40 \leq Y^+ \leq 1000$ possible points		$40 \leq Y^+ \leq 1000$ Max. points (17 points)
	# of points	Erravg. (%)		# of points	Erravg. (%)	
HB	21	8.8	31.6	9	12.4	50.7
SRC	22	10.1	29.4	10	11.9	44.9
local_alpha	18	6.8	40.1	6	4.5	64.2
global_alpha	20	7.1	33.6	8	5.5	52.7
Inv._local_alpha	25	8.8	21.9	13	15.5	31.4
Inv._global_alpha	28	7.7	7.7	16	2.2	2.2